

## Time Scales and Spatial Patterns of Passive Ocean–Atmosphere Decay Modes\*

BENJAMIN R. LINTNER AND J. DAVID NEELIN

*Department of Atmospheric and Oceanic Sciences, and Institute of Geophysics and Planetary Physics, University of California, Los Angeles, Los Angeles, California*

(Manuscript received 23 February 2007, in final form 7 September 2007)

### ABSTRACT

The decay characteristics of a mixed layer ocean passively coupled to an atmospheric model are important to the response of the climate system to stochastic or external forcing. Two salient features of such decay—the spatial-scale dependence of sea surface temperature anomaly (SSTA) decay time scales and the spatial inhomogeneities of SSTA decay modes—are addressed using intermediate-level complexity and simple analytic models of the tropical atmosphere. As expected, decay time scales increase with the spatial extent of the SSTA. Most modes decay rapidly—with characteristic decay times of 50–100 days for a 50-m mixed layer—with the decay determined by local surface flux adjustment. Only those modes with spatial scales approaching or larger than the tropical basin scale exhibit decay time scales distinctively longer than the local decay, with the decay time scale of the most slowly decaying mode of the order of 250–300 days in the tropics (500 days globally). Simple analytic prototypes of the spatial-scale dependence and the effect of basic-state inhomogeneities, especially the impact of nonconvecting regions, elucidate these results. Horizontal energy transport sets the transition between fast, essentially local, decay time scales and the slower decay at larger spatial scales; within the tropics, efficient wave dynamics accounts for the small number of slowly decaying modes. Inhomogeneities in the basic-state climate, such as the presence or absence of mean tropical deep convection, strongly impact large-scale SSTA decay characteristics. For nonconvecting regions, SSTA decay is slow because evaporation is limited by relatively slow moisture divergence. The separation of convecting- and nonconvecting-region decay times and the closeness of the slower nonconvecting-region decay time scale to the most slowly decaying modes cause a blending between local nonconvecting modes and the large-scale modes, resulting in pronounced spatial inhomogeneity in the slow decay modes.

### 1. Introduction

Coupling of the ocean–atmosphere system is an important facet of climate system variability relevant to adjustment processes and teleconnections. It is conceptually useful to distinguish the following two types of ocean–atmosphere coupling: “active” and “passive.” The former involves changes to ocean circulation (e.g., surface wind stress forcing or thermocline dynamics) that impact surface temperatures and feedback to the atmosphere. Active coupling plays a crucial role in the evolution and dynamics of El Niño–Southern Oscilla-

tion (ENSO; Philander et al. 1984; Cane and Zebiak 1986; Battisti 1988; Neelin et al. 1998; and references therein), as interactions of the thermocline, equatorial ocean wave dynamics, surface fluxes, and convection dictate the spatial extent and time scales of ENSO events. Active coupling has been further implicated in the low-frequency variability of the extratropical sea surface temperature anomalies (SSTAs), with oceanic Rossby wave dynamics and the thermohaline and wind-driven circulations contributing to the development of spatially coherent modes of SSTA variability on interdecadal and longer time scales (Münnich et al. 1998; Neelin and Weng 1999; Gallego and Cessi 2001; Marshall et al. 2001).

Passive ocean–atmosphere coupling is simpler, as it involves only thermodynamically mediated changes to ocean heat storage. For a net surface flux  $F_{\text{NET}} = E + H + R_S$ , where  $E$  is latent heating (evaporation),  $H$  is sensible heating, and  $R_S$  is the net surface longwave plus shortwave radiative heating, the time evolution of a passively coupled mixed layer is simply

\* Institute of Geophysics and Planetary Physics Contribution Number 6310.

*Corresponding author address:* Dr. Benjamin R. Lintner, Department of Atmospheric and Oceanic Sciences, University of California, Los Angeles, 405 Hilgard Ave., 7127 Math Science Bldg., Los Angeles, CA 90095-1565.  
E-mail: ben@atmos.ucla.edu

$$c_M \partial_t T_s = F_{\text{NET}}, \quad (1)$$

where  $T_s$  is the mixed layer temperature and  $c_M$  is the mixed layer heat capacity. The use of passive coupling is well known from studies of the extratropical SST response to short time-scale atmospheric forcing (Hasselmann 1976; Frankignoul and Hasselmann 1977; Barsugli and Battisti 1998). In the simple stochastic models of Hasselmann (1976) and Frankignoul and Hasselmann (1977),  $F_{\text{NET}}$  is just

$$F_{\text{NET}} = -\epsilon_{T_s}^{\text{net}} T_s + \phi, \quad (2)$$

where the first term on the right-hand side is the net effect of (negative) surface heat flux feedbacks; that is,  $\epsilon_{T_s}^{\text{net}}$  ( $>0$ ) is a damping coefficient representing the net surface heat flux anomaly per unit  $T_s$  anomaly and  $\phi$  is the net heat flux associated with stochastic “weather noise” forcing.

In the tropics, passive coupling also plays a significant role, especially in the context of tropical teleconnections (Klein et al. 1999; Saravanan and Chang 2000). The thermal inertia of the ocean mixed layer delays the remote surface temperature response to El Niño, which in turn impacts tropospheric warming and precipitation (see, e.g., Chang et al. 1998; Alexander et al. 2002; Giannini et al. 2001; Chiang and Sobel 2002; Tang and Neelin 2004; Neelin and Su 2005; Su et al. 2005, hereafter SNM05; Chiang and Lintner 2005). Studies of other coupled tropical phenomena, including intraseasonal variability and the Madden–Julian oscillation, further demonstrate the potential impacts of passive coupling (Sobel and Gildor 2003; Maloney and Sobel 2004; Grabowski 2006; Zhang et al. 2006). Passive coupling also modulates the transient response to global warming (Chou and Neelin 2004; Chou et al. 2006).

The form of  $F_{\text{NET}}$  in (2) is reasonable for the mid-latitudes, where the effect of surface fluxes on the atmosphere may be neglected on sufficiently short time scales. Within the tropics, however, strong “two-way” coupling between the surface and atmosphere necessitates explicit treatment of atmospheric conditions. To that end, SNM05 considered a simple, passively coupled tropical ocean–atmosphere analog to the Hasselmann model with tropospheric temperature  $T$  representing the state of the tropical atmosphere:

$$c_M \partial_t T_s = -\epsilon_{T_s}^{\text{net}} T_s + \epsilon_{\text{sfc}}^{\text{net}} T \quad (3)$$

$$c_A \partial_t T = -[\epsilon_{\text{toa}}^{\text{net}} + \epsilon_{\text{tr}}^{\text{net}} + (1 - \sigma_L) \epsilon_{\text{sfc}}^{\text{net}}] T + (1 - \sigma_L) \epsilon_{T_s}^{\text{net}} T_s. \quad (4)$$

Here,  $c_A$  is tropospheric heat capacity and  $\sigma_L$  is the fraction of tropical land area. The damping coefficient  $\epsilon_{T_s}^{\text{net}}$  is defined slightly differently than in (2): here it

represents the net surface flux anomaly per  $T_s$  when  $T$  is fixed. Also,  $\epsilon_{\text{sfc}}^{\text{net}}$  comes from the linearization of the net surface flux with respect to  $T$  perturbations, assuming  $T_s$  is fixed; similarly,  $\epsilon_{\text{toa}}^{\text{net}}$  is associated with linearization of the top-of-the-atmosphere net radiative heating with respect to  $T$ . The term in  $\epsilon_{\text{tr}}^{\text{net}}$  comprises the total effect of advective and diffusive (eddy) atmospheric energy transport.

Equations (3) and (4) are characterized by *uncoupled* decay time scales  $c_M \epsilon_{T_s}^{\text{net}-1}$  and  $c_A [\epsilon_{\text{toa}}^{\text{net}} + \epsilon_{\text{tr}}^{\text{net}} + (1 - \sigma_L) \epsilon_{\text{sfc}}^{\text{net}}]^{-1}$  for the ocean and atmosphere components, respectively. On the other hand, the slow *coupled* decay time scale of the tropical ocean–atmosphere system, on the scale of the whole tropics,

$$\tau_G = c_M \epsilon_{T_s}^{\text{net}-1} [1 + (1 - \sigma_L) \epsilon_{\text{sfc}}^{\text{net}} (\epsilon_{\text{toa}}^{\text{net}} + \epsilon_{\text{tr}}^{\text{net}})^{-1}], \quad (5)$$

is longer than the uncoupled decay time scales of either the atmosphere or ocean. For reference, SNM05 estimated a value for  $\tau_G$  of roughly 260 days for a 50-m mixed layer.

In a strict sense, the SNM05 model applies only to coupled mode decay for tropical mean conditions, and in later sections, we consider local analogs of (5). However, we can anticipate here some of the effects encountered in the extension of (5) to local scales. Since the tropical basic-state climate is spatially inhomogeneous, locally estimated damping time scales may deviate substantially from the tropical mean value: regional differences in the damping, exchange, and feedback coefficients (e.g., turbulent flux wind speed dependences) may lead to pronounced differences in local decay times. Park et al. (2005) estimated the surface heat flux response to SSTAs and found regional differences of the order  $25 \text{ W m}^{-2} \text{ K}^{-1}$ , although intratropical differences tend to be smaller. Inhomogeneities in ocean mixed layer depth also modulate regional decay characteristics, with mixed layer depths ranging over an order of magnitude both geographically and seasonally (Kara et al. 2003).

The spatial-scale dependence of decay time scales complicates the study of passive ocean–atmosphere coupling. Previous studies (e.g., Bretherton 1982; Frankignoul 1985; Schopf 1985; Marotzke and Pierce 1997; Nilsson 2001; SNM05) considered the effect of anomaly size on SSTA decay characteristics and identified decay regimes set by physics at various scales. For sufficiently localized anomalies, decay times are set by local surface exchange coefficients. On the other hand, at the largest scales, decay is limited by top-of-the-atmosphere outgoing longwave radiation. Since a key aspect in the transition between scales is the efficiency of net energy export away from an anomaly, the consideration of Eq. (5) is again instructive. The  $\epsilon_{\text{tr}}^{\text{net}}$  term

approximates horizontal energy flux (per  $T$ ) across a domain boundary, divided by the area of the domain. For a sufficiently localized SSTA,  $\epsilon_{\text{tr}}^{\text{net}} \gg \epsilon_{\text{sfc}}^{\text{net}}$ , since atmospheric heat transport away from the anomaly is large compared to  $T$ -mediated surface flux adjustment; from (5), this implies decay on a time scale comparable to an uncoupled mixed layer. On the other hand, as the size of the SSTA increases, the efficiency of heat transport is diminished; in the limit  $\epsilon_{\text{tr}}^{\text{net}} \ll \epsilon_{\text{toa}}^{\text{net}}$ , the decay time scale is (setting  $\sigma_L = 0$  for simplicity)  $\tau_G = c_M \epsilon_{T_s}^{\text{net}^{-1}} [1 + \epsilon_{\text{sfc}}^{\text{net}} \epsilon_{\text{toa}}^{\text{net}^{-1}}]$ . Since  $\epsilon_{\text{toa}}^{\text{net}}$  is small compared to  $\epsilon_{\text{sfc}}^{\text{net}}$  the decay of large-scale SSTAs is slow relative to more localized anomalies. While this simple picture contains much that is correct, the explicit inclusion of local physics, especially moist dynamics, has nontrivial consequences. In the tropics, horizontal transports are accomplished largely by planetary wave dynamics, with local tropospheric warming driven primarily by moist convection and remote warming occurring through compensating descent. The ascending and descending circulations interact with the tropospheric moisture field, which (as we will see below) has significant implications for the decay characteristics of convecting and nonconvecting regions.

Given the apparent relevance of passive ocean–atmosphere coupling to climate variability, we develop here a general framework for understanding the spatiotemporal characteristics of SSTAs as simulated by atmospheric models thermodynamically coupled to a mixed layer. A basic assumption is that the adjustment of the coupled mixed layer–troposphere system can, to first approximation, be projected onto a set of decay modes. (For the ENSO teleconnection or global warming problems, the “decay” is actually a forced response to a new equilibrium.) With this in mind, one approach taken here is to use an intermediate-level complexity model [the Quasi-Equilibrium Tropical Circulation Model 1 (QTCM1); see Neelin and Zeng (2000) and Zeng et al. (2000)] to compute a matrix of surface heat fluxes associated with a set of imposed SST perturbations; this surface heat flux matrix forms an eigenvalue problem from which decay modes are calculated. In the absence of basic-state inhomogeneities (e.g., for a uniform tropics), the slowest decay mode has a broad spatial scale; on the other hand, because of efficient wave dynamics, effectively all other modes decay at a much faster time scale—essentially, the uncoupled time scale associated with local surface flux adjustment. For a realistic basic state, by contrast, regional inhomogeneities (e.g., mean convecting versus nonconvecting conditions) modify decay time scales and their spatial signatures. Simple analytic prototypes are developed to gain

insights into the key features of modal time scales and spatial characteristics.

An obvious limitation of this study is that the absence of ocean dynamics means that some important physical mechanisms are neglected. However, we argue that the passive coupling framework is a highly useful (and, in fact, nontrivial) starting point, worth establishing in its own right, especially as an aid to understanding the interaction of these modes with active coupling phenomena such as ENSO. Another potential limitation is that the QTCM1 framework may overly simplify the physics involved. While a valid concern, we point out that QTCM1 has been applied successfully to many other problems in tropical climate dynamics, at least relative to other models (see, e.g., Chou and Neelin 2004; Neelin and Su 2005; SNM05; Chiang and Lintner 2005). In fact, the simplicity of QTCM1 permits studies that are far more challenging to carry out with GCMs, both diagnostically and computationally. Although the results of the current study are based on a simple model, we envision future studies, similarly designed, to be carried out with GCMs: our approach here is thus intended as a template to guide such studies.

## 2. Autocorrelation function persistence analysis

In this section, we consider the decay characteristics of simulated SSTAs as estimated from the temporal autocorrelation coefficient (i.e., the lagged self-correlations of the SSTA field). Temporal autocorrelations have been widely used to infer the persistence or decay characteristics of observed SSTAs, especially in the extratropics (e.g., Bhatt et al. 1998; Kushnir et al. 2002; Watanabe and Kimoto 2000; Timlin et al. 2002; Deser et al. 2003). These studies suggest characteristic damping time scales for extratropical SSTAs of the order 90–180 days. Larger persistence values have also been noted, with mechanisms such as reemergence significantly increasing persistence (Deser et al. 2003).

The simulated SSTA field was obtained from version 2.3 of QTCM1 coupled to a constant-depth, 50-m mixed layer. While the reader is referred to Neelin and Zeng (2000) and Zeng et al. (2000) for detailed descriptions of the QTCM1 framework, we note here that the model consists of a Galerkin-like vertical projection of the primitive equations onto vertical structures tailored to tropical deep convection regions. A single temperature profile is implemented, consistent with the notion that convective quasi-equilibrium (QE) constrains the vertical structure of temperature in convecting regions and wave dynamics spreads this structure horizontally. Vertical basis functions for velocity are chosen to be consistent with barotropic and first baroclinic pressure gra-

dients, assuming the QE-constrained temperature profile. A single moisture basis function, broadly consistent with observed vertical humidity profiles in tropical convecting regions, is used. Physical processes, including radiative transfer, convective adjustment, and surface exchanges, are parameterized as in a GCM. The convective parameterization is the simple profile relaxation scheme of Betts and Miller (1986).

The output analyzed here consists of 10 independent simulations, each of 50-yr duration at a resolution of  $5.625^\circ \times 3.75^\circ$ . A “Q-flux” adjustment was applied to the net surface flux field to prevent systematic climate drift (Hansen et al. 1997). Since the forcings imposed on the model (i.e., top-of-the-atmosphere insolation, Q flux, land surface albedo) consisted of climatological monthly mean values, the simulated SSTA variability reflects QTCM1’s chaotic internal variability. For comparison, a similar experiment, though consisting of only a single, 85-yr integration, was carried out with the National Center for Atmospheric Research (NCAR) Community Climate Model version 3.10 (CCM3; see Kiehl et al. 1998) at T21 resolution. In what follows, we use as our measure of persistence (denoted  $\tau_p$ ) the lag for which the value of the SSTA autocorrelation coefficient falls to  $e^{-1}$ .

Overall, the  $\tau_p$  as simulated by QTCM1 and CCM3 manifest some gross similarities to one another (Fig. 1). In fact, the spatial pattern correlation coefficient of the two models’  $\tau_p$  fields is highly statistically significant (i.e.,  $r = 0.51$  for the entire ocean or 0.56 for  $30^\circ\text{S}$ – $30^\circ\text{N}$ ). Extremely long persistence times [ $\tau_p > 400$  days in CCM3 (Fig. 1b)] extend along the near-equatorial Pacific from  $\sim 150^\circ\text{W}$  eastward to the coastline of South America. While large  $\tau_p$  values are also evident in this region in QTCM1 (Fig. 1a), they barely exceed 300 days. Lengthy persistence is also evident in the southeast tropical Atlantic, and to a lesser extent the south Indian Ocean and high latitudes of both hemispheres. Short persistence times, on the order of 30–60 days, occur in the north Indian Ocean, the South Atlantic tropical convergence zone, and in an arc-shaped region of the western Pacific encompassing the South Pacific convergence zone and the western Pacific warm pool. A prominent regional discrepancy between the two models occurs in the tropical Atlantic immediately north of the equator: CCM3 exhibits a zonally elongated local maximum, with  $\tau_p$  values around 200 days, while QTCM1 fails to produce such high values. Although the exact nature of this discrepancy (or others) is unclear, it is likely related to differences in model physics, such as the treatment of the planetary boundary layer or turbulent flux parameterizations.

We point out that the geographic distribution of

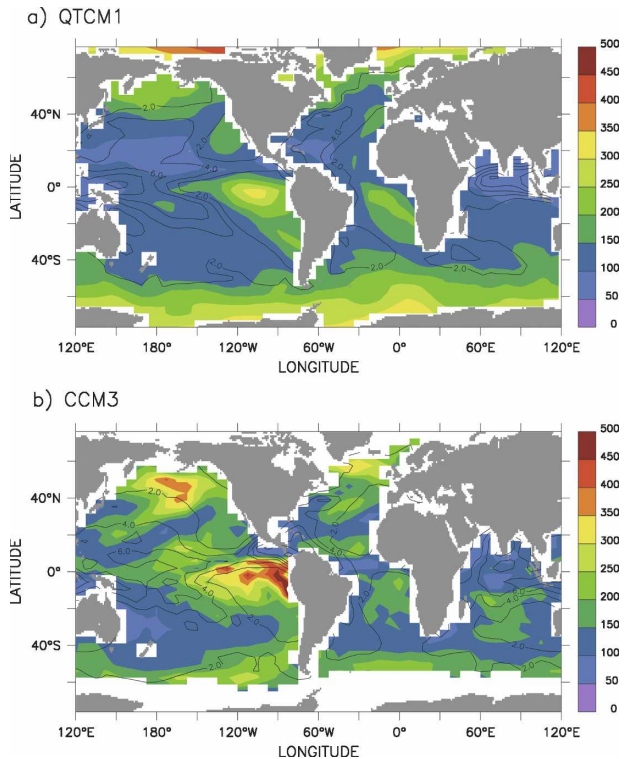


FIG. 1. Lagged autocorrelation persistence times (days) for 50-m global mixed layer simulations of (a) QTCM1 and (b) CCM3. Values plotted correspond to the time for the autocorrelation function to fall to  $e^{-1}$ . Also shown are contours of time-mean precipitation ( $\text{mm day}^{-1}$ ).

tropical  $\tau_p$  broadly resembles the distribution of mean convection, especially in QTCM1 (Fig. 1, line contours, in units of  $\text{mm day}^{-1}$ ). The regions of weakest mean oceanic convection—the eastern equatorial Pacific, the southeast Atlantic, and south Indian Ocean—exhibit some of the most persistent mixed layer SSTA variability in the tropics. In section 5, we explore the origins of the long persistence/slow decay of nonconvecting-region SSTAs using a simplified analytic framework.

It is worth noting the possible relationship of the passively coupled  $\tau_p$  simulated here to observed autocorrelation persistence in the tropics. As demonstrated by previous studies, the spatial structure of tropical  $\tau_p$  is strongly influenced by ENSO (cf. Fig. 2 of Wu and Newell 1998): in particular, long persistence times, on the order of 200 days or more, are noted in the equatorial eastern Pacific source region of ENSO as well as those remote regions strongly teleconnected to ENSO (e.g., the north tropical Atlantic and the western Indian Ocean basins). We find it intriguing that the passively coupled simulations manifest lengthy persistence in the ENSO source region, even though the ocean dynamics responsible for ENSO are absent. It seems plausible

that the slow decay regime prevailing in the eastern Pacific in the passive coupling framework interacts with the active dynamics responsible for ENSO, thereby affecting such features as the frequency, duration, and magnitude of ENSO events. However, the details of this interaction are beyond the scope of the present study.

Apart from the spatial structure of  $\tau_p$ , it is also of interest to address what happens to the decay characteristics as successively larger spatial scales are considered. Remote coupling of localized patches of SSTAs, via the atmosphere, may substantially alter decay times, following the arguments in section 1. To reiterate, as the spatial extent of the anomalies—or the spatial extent of anomaly correlations—increases, the persistence time lengthens (or the rate of decay slows) because the efficiency of net local energy export is reduced. Indeed, simple spatial aggregation of SSTA hints at the lengthening of  $\tau_p$  as larger regions are considered. For example, for QTCM1, the mean, gridpoint-averaged  $\tau_p$  for the entire tropics (30°S–30°N) is roughly 125 days. On the other hand, the decay time estimated from the tropical-mean SSTA is nearly 200 days. (The  $\tau_p$  estimate of the global-averaged ocean is 315 days.) Similar scaling behavior occurs in the CCM3 simulation, albeit with a more pronounced increase of  $\tau_p$  at larger scales.

### 3. Eigenvalue analysis

Interpretation of the decay characteristics derived from autocorrelation persistence is subject to some ambiguity. Even though the autocorrelations are computed pointwise, they reflect both local and remote influences. In fact, the decay characteristics of a localized SSTA depend implicitly on the behavior of remote regions (e.g., a warm anomaly of given magnitude decays more rapidly if it occurs in isolation than if it occurs as part of a broader pattern of warm anomalies). Also, the single value estimate of  $\tau_p$  belies the fact that the decay typically arises from an interplay of multiple decay time scales. In light of these complexities, an approach that takes into account the modal nature of passive SSTA decay is clearly desirable. Here, we present one such approach, a simple eigenvalue analysis.

#### a. Method

To implement the eigenvalue analysis, the oceanic domain is subdivided into  $N$  regions that form a basis of an  $N$ -dimensional subspace of SST anomalies. An SST perturbation within the  $j$ th basis region induces an anomalous surface heat flux response in the  $i$ th basis

region ( $\Delta F_i$ ). Considering an arbitrary distribution of SSTAs and their associated surface heat flux anomalies, the time evolution of the perturbation surface temperature field can be written as

$$c_{M_i^k} \partial_t \Delta T_{sk} = G_i^j \Delta T_{sj}, \quad (6)$$

where  $c_{M_i^k}$  is a diagonal matrix of basis region heat capacities and  $G_i^j$  is a sensitivity matrix relating  $\Delta F_i$  to  $j$ th basis region perturbation forcing. It is straightforward to solve Eq. (6) as a simple matrix eigenvalue problem; the general time-dependent solution for an arbitrary distribution of surface temperature perturbations  $\mathbf{T}_s(\mathbf{0})$  is (in matrix notation)

$$\Delta \mathbf{T}_s(\mathbf{t}) = \mathbf{V} \mathbf{D} \mathbf{V}^{-1} \mathbf{T}_s(\mathbf{0}), \quad (7)$$

where  $\mathbf{V}$  is the eigenvector matrix of  $\mathbf{c}_M^{-1} \mathbf{G}$  and  $\mathbf{D}$  is a diagonal matrix with elements  $e^{-\lambda_i t}$ , with the  $\lambda$ 's representing the eigenvalues of  $\mathbf{c}_M^{-1} \mathbf{G}$ .

QTCM1 was used to estimate the sensitivity matrix  $\mathbf{G}$ . For the  $j$ th basis region, an ensemble of model integrations was obtained assuming a 1-K SSTA applied in the  $j$ th region and zero elsewhere. From the difference in net surface heat fluxes, averaged over December–February,  $\mathbf{G}$  was calculated for each basis region simulation relative to a control simulation in which no SST perturbations were applied. The analysis presented below considers either  $N = 5$  (“basin scale”) or  $N = 35$  (“subbasin scale”), with an ensemble size of 40. For  $N = 5$ , the basis regions consisted of the three principal tropical ocean basins between 30°S and 30°N, the Pacific (PAC), Atlantic (ATL), and Indian (IND), as well as the entire Northern and Southern Hemisphere extratropical ocean for latitudes poleward of 30° (NH EXT and SH EXT). For  $N = 35$ , the PAC, ATL, and IND basis regions were further subdivided into 19, 8, and 6 regions, respectively. The extratropical basis regions are kept the same, since our principal interest is understanding the finer-scale structure of tropical decay characteristics. Unless otherwise stated, the results discussed represent the eigenvalue analysis applied to the ensemble average of  $\mathbf{G}$ . For simplicity, a constant, 50-m mixed layer was assumed.

It should be emphasized that an underlying assumption of the eigenvalue approach is that the net surface flux responses associated with each basis region are linearly additive. In other words, for any arbitrarily defined patch of ocean surface  $\Omega$ , the product  $G_\Omega^j \Delta T_{sj}$  (where the flux response per SST perturbation in the  $j$ th region is here averaged over  $\Omega$ ) should be independent of how the oceanic domain is partitioned into basis regions. However, from previous studies (e.g., Su et al. 2003), we expect that nonlinearities may be encoun-

TABLE 1. Summary of the  $N = 5$  eigenvalue analysis. Values tabulated in columns 2–5 are modal decay times, in days, estimated from the ensemble mean of  $\mathbf{G}$  (column 2); 95% confidence intervals for the ensemble-mean decay times, in days, estimated from a simple bootstrapping with replacement scheme (column 3); dimensionless spatial means of the modal eigenvectors (column 4); and dimensionless spatial standard deviation of the modal eigenvectors (column 5). Note that for complex modes, the period of the oscillatory component appears in parentheses beside decay time. Column 6 gives the decay time (in days) estimated from the mean of the eigenvalue analysis applied to individual ensemble members, with  $\pm 1\sigma$  values of the mean also provided. For comparison, local decay times from the diagonal elements of the sensitivity matrix  $\mathbf{G}$  for the five regions are  $384.7 \pm 14.2$  (SH EXT),  $184.6 \pm 39.5$  (PAC),  $156.6 \pm 29.4$  (NH EXT),  $128.0 \pm 20.1$  (ATL), and  $110.1 \pm 9.7$  (IND).

Mode	Decay time	95% confidence interval	Eigenvector mean	Eigenvector standard deviation	Intraensemble decay time
1	495.4	478.7–513.9	0.36	0.29	$507.2 \pm 79.7$
2	256.3	248.3–264.3	0.25	0.42	$259.8 \pm 33.6$
3	128.1	118.4–136.9	0.06	0.50	$139.1 \pm 23.8$
4	107.0 (4625.8)	103.7–110.9	$0.01 - 0.01i$	0.50	$109.1 \pm 12.9$
5	107.0 (4625.8)	103.7–110.9	$0.01 + 0.01i$	0.50	$101.7 \pm 9.3$

tered, especially as the size of basis regions is reduced. In particular, with decreasing basis region area, nonlinear impacts from SST gradients at the edges of the region become more apparent.

To assess the linearity constraint, we compared the global distribution of summed net surface flux anomalies for both the basin- and subbasin-scale partitionings to the pattern of global net surface flux anomalies for a globally specified 1-K SST anomaly (i.e.,  $N = 1$ ). While the  $N = 5$  case manifests some nonlinearity, especially at the gridpoint scale, the agreement for the  $N = 1$  and  $N = 5$  averages over the basis regions was within 20%. On the other hand, for  $N = 35$ , deviations from linearity at the scale of the basis regions were found to be much larger, especially in the vicinity of the Northern Hemisphere midlatitude winter storm tracks. Of course, this region is subject to considerable baroclinic instability, so the strong nonlinear response is not surprising.

To mitigate nonlinearities, we implemented two changes for the  $N = 35$  analysis relative to that for  $N = 5$ . First, we reduced the amplitude of the perturbation SST forcing from 1 to 0.2 K. Reducing the forcing amplitude not only decreases the magnitude of SST gradients but also diminishes the impact of nonlinearities in other physical processes (e.g., the relationship between SST and surface specific humidity). Of course, lowering the forcing amplitude decreases signal-to-noise ratios, which may be compensated by increasing the size of the ensemble. Second, we modified QTCM1's temperature and moisture advection scheme to limit the effect of baroclinic instability. In particular, temperature/moisture advection were replaced by their climatological mean values plus contributions from anomalous temperature and moisture gradients advected by mean winds. Contributions to temperature/moisture advection from mean gradients advected by

anomalous winds as well as anomalous gradient advection by anomalous winds were suppressed. Lin et al. (2000) employed a similar approach in their study of tropical intraseasonal variability to suppress high-frequency contributions from midlatitude storms and noted that the leading features of tropical climate dynamics were hardly affected. We emphasize that we consider the results for the large-scale modes to be more accurately evaluated from the  $N = 5$  case but that the  $N = 35$  case (with the aforementioned modifications) is broadly consistent at the large scale.

#### b. Eigenvalue analysis applied to basin-scale SST forcing

The leading eigenmode (mode 1) for the  $N = 5$  eigenvalue analysis is characterized by a decay time scale of nearly 500 days (Table 1, column 1). This decay time exceeds the area-weighted mean of basin-scale local decay times, estimated from the diagonal entries of  $\mathbf{G}$ , by 270 days. Mode 1 clearly reflects enhanced persistence (or slower decay) relative to locally estimated decay. Examination of the sensitivity matrix elements immediately suggests why this is the case: while the diagonal entries of  $\mathbf{G}$  are negative—corresponding to SSTA decay within the region in which the SST perturbation is imposed—the off-diagonal entries are typically (though not always) positive—that is, the mixed layer tends to warm away from the location of the imposed SSTA. Flux cancellation between diagonal and off-diagonal matrix elements results in at least one eigenmode with a decay time scale exceeding the local decay values.

Spatially, mode 1 manifests the broadest, most uniform spatial structure, as evidenced by its relatively large spatial mean and small spatial standard deviation. However, while the projection of the leading mode is of the same sign in all regions, the loading varies by a factor of 4 across the five basis regions, with its stron-

gest projection in the SH EXT region, where the local decay time is largest. The lengthy decay of the SH EXT region may simply reflect its large overall area and low land-to-ocean ratio: longer decay is expected based on the size of the SSTA and the fact that the ocean surface area is large compared to the radiating area of the top-of-the-atmosphere. In any event, the spatial heterogeneity of the slowest decay mode reflects variations in basic-state climatology: the leading eigenmode convolves the broad scales anticipated for the most slowly decaying mode with localized regions of slow decay.

The remaining eigenmodes exhibit decay characteristics reflecting the local decay features. For instance, the second mode decay time ( $\sim 260$  days) lies between the decay time of SH EXT and the remaining regions. The second eigenvector is of one sign in SH EXT and of opposite sign elsewhere. (Mode 3 behaves similarly, but with the projection of one sign in PAC and opposite sign elsewhere.) The decay times of modes 4 and 5 are seen to be complex conjugates, indicating oscillatory decaying behavior rather than strict exponential decay. However, since the period of oscillation is much longer than the decay time, the complex modes are strongly overdamped and thus behave essentially like exponentially decaying modes.

One consideration in the interpretation of the eigenvalue analysis is the statistical significance of the eigenmodes (e.g., how robust are the modal decay time scales?). Quantitative insight into statistical significance was obtained through a simple bootstrapping with replacement scheme (Efron 1982). Following standard procedure, 1000 bootstrap  $\mathbf{G}$  matrices were generated by averaging 40 individual  $\mathbf{G}$  matrices drawn at random from the available simulated data. Eigenvalues of the bootstrap matrices were then computed and sorted, and a two-sided 95% confidence interval for each modal decay time was estimated from the 25th and 975th values (Table 1, column 3).

Overall, the bootstrapping analysis underscores very stable eigenvalues at the basin scale. For each mode, the width of the confidence interval is less than 10% of the ensemble-mean decay time scale. The bootstrapping results appear to be broadly consistent with uncertainty estimates based on the eigenvalues estimated from the 40 individual members (Table 1, column 6). The latter provides some sense of how reliable estimates of decay characteristics would be for a single three-month average. For example, for the leading eigenmode, the intraensemble standard deviation is approximately 80 days. With an ensemble of 40, one would anticipate, assuming Gaussian-distributed, uncorrelated variance, an uncertainty of  $(80/40^{1/2}) \approx 13$

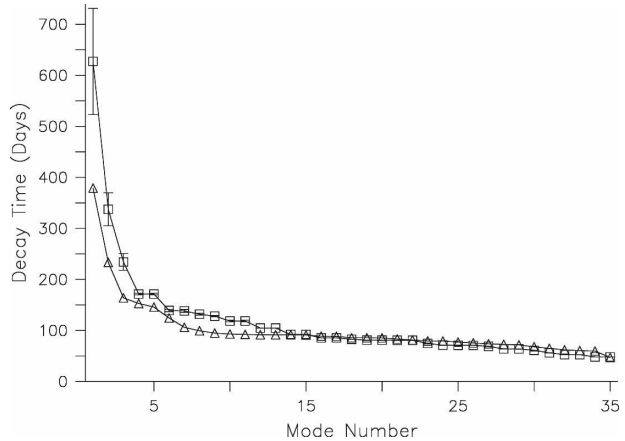


FIG. 2. Eigenmode decay times for the  $N = 35$  basis region eigenvalue analysis. Eigenmode decay times (days) are plotted as squares. The error bars shown are standard deviations of the modal decay times estimated from 1000 bootstrap samples. For comparison, local decay times, estimated from the diagonal entries of the flux sensitivity matrix  $\mathbf{G}$ , are also shown (triangles).

days, which falls within the 95% bootstrap confidence interval.

### c. Eigenvalue analysis applied to subbasin scales

We now turn to the  $N = 35$  eigenvalue analysis. Although our principal emphasis here is on tropical decay characteristics, the results discussed include the extratropics (the “global case”). It is necessary to view tropical SSTA decay in a global context since tropical–extratropical transports will potentially influence tropical decay characteristics. However, because QTCM1 is not optimized for extratropical dynamical accuracy, and the extratropics are incorporated into the analysis as spatially large basis regions, we will also consider what happens to the tropical decay characteristics when the extratropics are excluded from the analysis (the “tropics-only case”).

The spectrum of the real part of modal decay times for the global case, sorted from slowest to fastest, is illustrated in Fig. 2, with local decay time estimates displayed for comparison. The leading mode, with  $\tau_{\text{decay}} = 609$  days, lies well above any of the local decay estimates. The nonleading modal decay times, by contrast, fall below at least one of the local decay estimates. Also, as a consequence of the alteration to QTCM1’s advection scheme, the leading mode decay time for  $N = 35$  is approximately 115 days longer than the leading mode for  $N = 5$ .

Eigenvector loadings of the first three modes of the global case are displayed in Fig. 3. Like the leading eigenmode of section 3b, the leading mode (Fig. 3a)

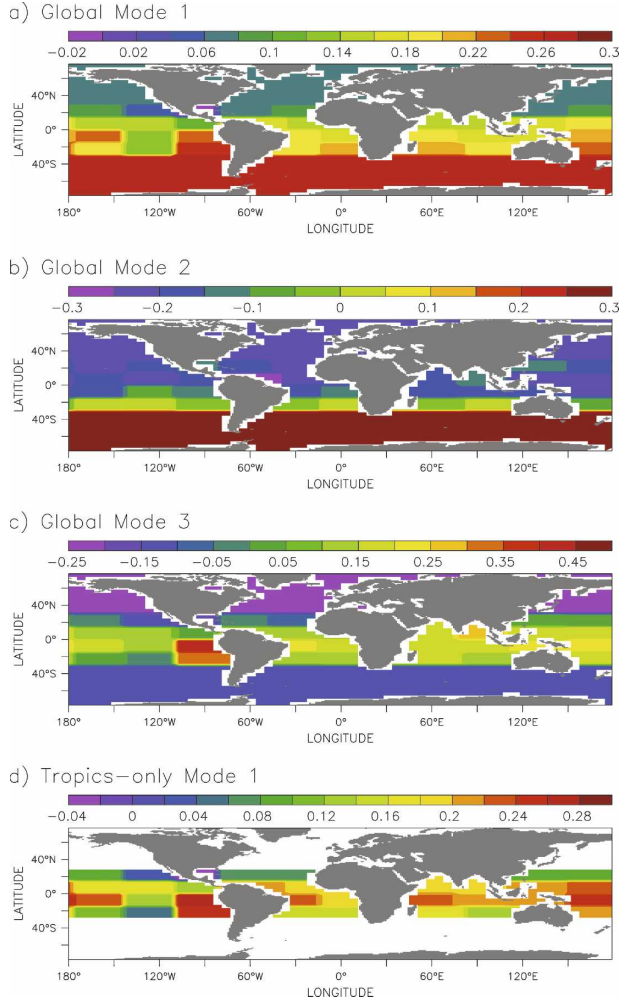


FIG. 3. Eigenmode spatial loadings of the (a) first, (b) second, and (c) third eigenmodes of the  $N = 35$  eigenvalue analysis and (d) the first eigenmode of the tropics-only ( $N = 33$ ) case. Note the difference in color bars among (a)–(d).

exhibits the lowest spatial standard deviation to spatial mean ratio, consistent with expectations of a broad structure for the slowest decay mode. While the first eigenvector loading is practically the same sign everywhere, the amplitude of the eigenvector is quite variable regionally, with the strongest loading in the SH extratropics. The structure of the leading eigenmode loading again underscores a relatively unclear separation between the slowly decaying, spatially broad mode and localized regions of slow decay. Mode 2 (Fig. 3b) is characterized by both positive and negative loadings; especially prominent is the sign difference between the extratropical Northern and Southern Oceans. The third mode (Fig. 3c) is positive throughout much of the tropics and negative in the northern and southern extratropics, and the region of slow local decay in the eastern Pacific is highly weighted.

The spatial projection of the leading eigenmode of the tropics-only case appears in Fig. 3d. Overall, the spatial features in Fig. 3d resemble those of mode 3 in the global case. The loadings in Fig. 3d, which are largely positive everywhere, exhibit especially large values in the southeastern tropical Pacific. Also, the tropics-only mode reflects a longer decay time than mode 3 (351 versus 230 days), since the effect of canceling fluxes in the extratropics is absent. Physically, the tropics-only configuration is of more relevance to forcing spread by equatorial wave dynamics (as in ENSO teleconnections), since modes 1 and 2 would require global- or hemispheric-scale forcing to be excited. In the remainder of the paper we address how the inhomogeneity in the basic state potentially influences decay time scales and spatial patterns in the tropics-only case.

#### 4. Analytic prototype for SST decay spatial-scale dependence

Following the approach of SNM05, we consider a set of (perturbation) equations for  $T_s$  and  $T$  as well as specific humidity ( $q$ ) for the tropical climate system:

$$c_M \partial_t T_s = \epsilon_s^{T_s} T_s + \epsilon_T^T T + \epsilon_q^T q + C_{T_s} P, \quad (8)$$

$$c_A \partial_t T = \epsilon_{T_s}^T T_s + \epsilon_T^T T + \epsilon_q^T q - M_s \nabla \cdot \bar{\mathbf{v}} - \bar{M}_s \nabla \cdot \mathbf{v} + P(1 + C_T), \quad (9)$$

$$c_A \partial_t q = \epsilon_s^q T_s + \epsilon_T^q T + \epsilon_q^q q + M_q \nabla \cdot \bar{\mathbf{v}} + \bar{M}_q \nabla \cdot \mathbf{v} - P. \quad (10)$$

Here, the coefficients  $\epsilon_j^k$  are generalized flux sensitivity coefficients (in units of  $\text{W m}^{-2} \text{K}^{-1}$ ; see appendix A for definitions) relating changes in the  $j$ th variable to the  $k$ th;  $M_s$  and  $M_q$  are dry static stability and moisture stratifications, respectively; and  $\nabla \cdot \mathbf{v}$  is the divergence. Convective heating and moistening in (9) and (10) are equal to the convective precipitation rate,  $P$ , with units of  $\text{W m}^{-2}$ . The terms in  $C_{T_s}$  and  $C_T$  in the  $T_s$  and  $T$  equations give the effect of total (shortwave plus longwave) cloud radiative feedback. Overbars denote prescribed mean-state values; all other values are assumed to be perturbations with respect to the mean state. The moisture is in units of K, absorbing  $L/c_A$  in  $q$ , and the time derivatives of  $T$  and  $q$ , shown here for completeness, are neglected in the analysis, since they are associated with fast atmospheric time scales. For later purposes, we define the gross moist stability  $M$  as  $M = M_s - M_q$ .

The  $T_s$ ,  $T$ , and  $q$  are regarded as functions of a generalized horizontal spatial coordinate,  $x$ . For simplicity, a homogeneous, convecting mean state (for which

$\nabla \cdot \bar{\mathbf{v}}=0$ ) is considered. The flux sensitivity coefficients are assumed spatially invariant, including the wind speed dependences in turbulent fluxes, and horizontal advection is ignored. In the Betts and Miller (1986) convective scheme,  $P = C_A(q - q_c)/\tau_c$ , where  $q_c$  is the convective reference humidity (treated here as a linear function of  $T$ ,  $q_c = \beta T$ , with  $\beta = 0.81$ ) and  $\tau_c$  is the convective adjustment time scale. In what follows, the strict QE limit (Neelin and Zeng 2000) of vanishingly small  $\tau_c$  is invoked. Strict QE implies  $q \rightarrow \beta T + \tau_c P/C_A$ , where  $P = \epsilon_{T_s}^p T_s + \epsilon_T^p T$ , with  $\epsilon_{T_s}^p = (\bar{M}_q \epsilon_{T_s}^T + \bar{M}_s \epsilon_{T_s}^q)/$

$(\bar{M} - C_T \bar{M}_q)$  and  $\epsilon_T^p = [\bar{M}_q(\epsilon_T^T + \beta \epsilon_q^T) + \beta \bar{M}_s \epsilon_q^q]/(\bar{M} - C_T \bar{M}_q)$ .

In addition to Eqs. (8)–(10), we consider a diagnostic momentum balance between the baroclinic pressure (temperature) gradient and (surface) friction:

$$r \partial_x T = \epsilon_u'' u. \quad (11)$$

Here,  $r$  is the gas constant for air ( $287 \text{ J kg}^{-1} \text{ K}^{-1}$ ) and  $\epsilon_u''$  is the net momentum damping. Assuming separable form solutions [i.e.,  $T_s(x, t) = \sum \tilde{T}_s e^{ikx/R_e} e^{\lambda t}$ ], we obtain a dispersion relationship of the form

$$\lambda = c_M^{-1} \left\{ \epsilon_{T_s}^T + C_{T_s} \epsilon_{T_s}^P - \frac{(\epsilon_{T_s}^T + \beta \epsilon_q^T - C_{T_s} \epsilon_T^P)(\epsilon_{T_s}^T + \epsilon_{T_s}^q + C_T \epsilon_{T_s}^P)}{[\epsilon_T^T + \beta(\epsilon_q^T + \epsilon_q^q) + C_T \epsilon_T^P](1 + k^2/k_0^2)} \right\}, \quad (12)$$

where  $R_e$  is the radius of the earth,

$$k_0 = R_e^{-1} \sqrt{\frac{[\epsilon_T^T + \beta(\epsilon_q^T + \epsilon_q^q) + C_T \epsilon_T^P] \epsilon_u''}{rM}},$$

and  $L_0 = R_e k_0^{-1}$  defines a characteristic length scale over which  $T$  anomalies behave coherently. The inverse of (12) is a generalized extension of (5).

Decay spectra for  $k_0 = 0, 1, 2$ , and  $3$  with and without cloud radiative feedback effects are illustrated in Fig. 4. For the active cloud radiative feedback (solid lines),  $C_T = 0.05$  and  $C_{T_s} = -0.17$ . In the inviscid limit  $\epsilon_u'' \rightarrow 0$ , the scale defined by  $L_0$  becomes infinite (i.e.,  $T$  fluctuations are uniform throughout the entire domain). In this weak temperature gradient (WTG) regime, SSTA decay at all nonzero wavenumbers is fast compared to the decay at wavenumber 0. For nonzero  $k_0$ , there is a smooth transition between the slowest decay mode at  $k = 0$  and the faster, effectively local decay values determined by  $\epsilon_{T_s}^T$  for  $k > k_0$ . For parameter values representative of the tropics in QTCM1 ( $M = 0.61 \text{ K}$ ,  $\epsilon_u'' = -0.1 \text{ day}^{-1}$ , and  $\epsilon_T^T = -33 \text{ W m}^{-2} \text{ K}^{-1} = -0.33 \text{ day}^{-1}$ ),  $k_0 \approx 1.5$ . Thus, we expect that only a small number of modes should exhibit decay time scales differing significantly from local decay values, in agreement with what is seen in Fig. 2.

Disabling the cloud radiative feedback (Fig. 4, dashed lines) increases the 1D prototype decay times, especially at nonzero wavenumber. The reason for this increase can be understood as follows: in the presence of the feedback, a warm  $T_s$  anomaly increases precipitation, and hence the fraction of deep convective clouds, over the SSTA. The increased cloud cover decreases the shortwave radiation incident on the surface (hence,  $C_{T_s} < 0$ ), which results in cooling, or faster decay than when the feedback is absent. The cloud ra-

diative feedback effect becomes less pronounced as the areal extent of the SSTA increases because the precipitation response per unit  $T_s$  is diminished since the term in  $\epsilon_{T_s}^p$  opposes the term in  $\epsilon_T^p$ .

The diagnostic balance between baroclinic gradients and frictional damping admits real (and decaying) solutions for  $\lambda$ . However, other balances are plausible (e.g., baroclinic pressure gradients and momentum advection). In general, this balance yields complex solutions for  $\lambda$  (i.e., solutions that propagate as well as decay). Previously, Nilsson (2001) presented a framework for understanding feedbacks between midlatitude stationary atmospheric waves and SSTAs that is relevant to such decaying, propagating solutions. Such solutions are likely to be of importance to a number of issues beyond the scope of this paper, including the development, maintenance, and timing of interbasin adjustment processes in the tropics.

## 5. Analytic prototype for differences between convecting and nonconvecting regimes

The prototype developed in this section offers insight into the separation between the fast local decay times of tropical convecting regions and the slow local decay of nonconvecting regions. The prototype also sheds light on the interpretation of the eigenvalue analysis (section 3), specifically for understanding the blending that occurs between the broad-scale, slow decay modes and the slow, local decay times characteristic of tropical nonconvecting regimes.

### a. The $N$ -box WTG model

Consider discretization of Eqs. (8)–(10) (again assuming WTG) over a domain consisting of  $N$  boxes

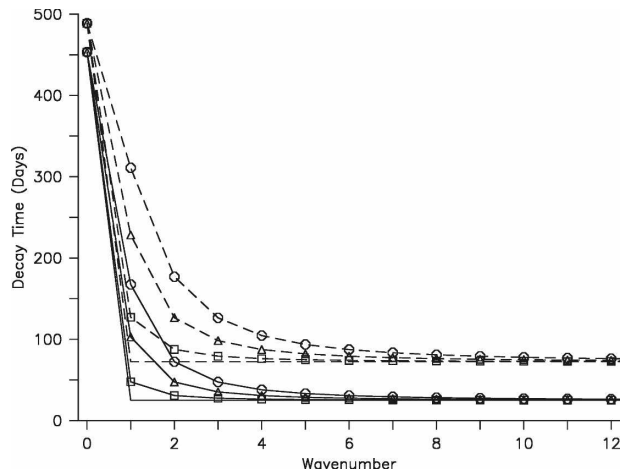


FIG. 4. Decay time dispersion relationship for the continuous 1D steady-state model. Shown are values with and without cloud radiative feedback (solid and dashed lines, respectively) for the inverse damping length wavenumber  $k_0$  of 0 (no symbols), 1 (squares), 2 (triangles), and 3 (circles). Note that the dispersion curve for values representative of the tropics in QTCM1 lies between  $k_0 = 1$  and  $k_0 = 2$  curves.

without the cloud radiative feedback. Numerical solution of these equations under SSTA forcing analogous to the eigenvalue analysis of section 3 (i.e., imposing unit SSTAs separately in each of the boxes) yields an  $N \times N$  atmospheric heat flux matrix, from which eigenvalues are computed. We are interested in what happens when convection is varied within a subset  $N_{pc}$  of the boxes, with a parameter  $\alpha_c$  denoting the convective fraction within the subset. One interpretation of  $\alpha_c$  is that it represents the time the  $N_{pc}$  subset spends convecting; alternatively, it can represent the spatial fraction of  $N_{pc}$  experiencing deep convection. The limit  $\alpha_c = 0$  corresponds to nonconvecting conditions;  $\alpha_c = 1$  is fully convecting limit, with all  $N$  boxes identical. Eigenvalues of these simulations, as a function of  $\alpha_c$ , are illustrated in Fig. 5a for  $N = 4$  and  $N = 8$  total boxes, and  $N_{pc} = 1$  and  $N_{pc} = 2$ , respectively. Here, we refer to the subset  $N_{pc}$  as the “partially convecting region.”

Consider the limit  $\alpha_c = 1$ , which corresponds to the leftmost points in Fig. 5a. For both  $N = 4$  and  $N = 8$ , there are two eigenvalues. The mode with the smaller eigenvalue, or slower decay time, projects uniformly into each box; we refer to this slow decay mode as the “global” or “G” mode. The remaining modes, the “local convecting” (LC) modes, are  $(N - 1)$ -fold degenerate and decay significantly faster than the G mode. The eigenvectors of the LC modes are approximately sinusoidal, although the finite size of the boxes modifies their spatial characteristics.

As  $\alpha_c$  is decreased, distinct eigenvalues emerge for

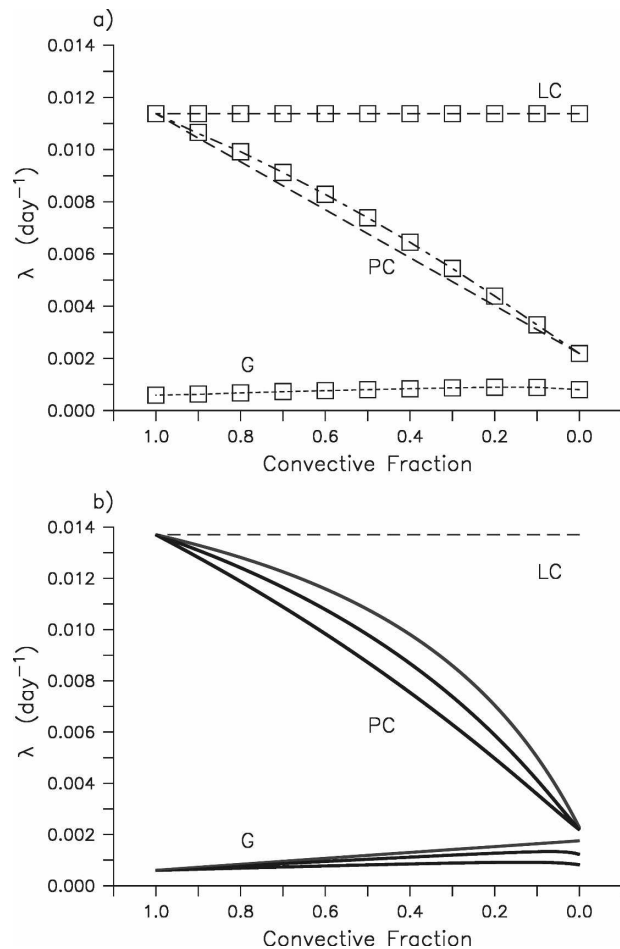


FIG. 5. Eigenvalues for (a) numerical  $N$ -box and (b) analytic two-box models as a function of the convective fraction  $\alpha_c$  in the partially convecting region. In (a), results are for  $N = 4$  and  $N = 8$  boxes (squares and dashed lines, respectively) for  $f_1 = 0.75$ . In (b), results are for  $f_1 = 0.75$  (black), 0.5 (dark gray), and 0.33 (light gray). The labels “G,” “PC,” and “LC” denote global decay mode, the mode(s) associated with the partially convecting region, and the local decay modes in the fully convecting region, respectively. In (a), the LC modes are either  $N - 1$  degenerate (for  $\alpha_c = 1$ ) or  $N - (N_{pc} + 1)$  degenerate (otherwise), while the PC modes are  $N_{pc}$  degenerate. In (b), the LC modes are computed from the two-box model with  $\alpha_c = 1$  (i.e., the entire tropics is fully convecting).

the partially convecting region. For  $N = 4$ , a single mode with a decay time scale intermediate between the LC and G modes emerges; for  $N = 8$ , there are two such modes since  $N_{pc} = 2$ . In what follows, we refer to these modes as the partially convecting (PC) modes. In the  $\alpha_c = 0$  limit, we also use the term “nonconvecting” (NC) modes. The PC eigenvector loadings are largely confined to the partially convecting region, and the eigenvalues, which are not strictly degenerate for  $N_{pc} > 1$ , remain close to one another even as the decay times vary significantly over the range of  $\alpha_c$ . The similarity of

PC modal decay rates for small  $\alpha_c$  means that the partially convecting-region decay times are relatively insensitive to the size of the SSTA within the partially convecting region, a point to which we return below.

The LC eigenvalue changes little as  $\alpha_c$  is varied. The G mode eigenvalue also varies only slightly with  $\alpha_c$ , partly because the partially convecting region is a relatively small portion of the total domain but also for reasons elaborated below. When  $\alpha_c$  is small, the PC decay times become comparable to the G mode decay time. As a result, the eigenvectors of the G and PC modes are altered in such a way that they become less distinct (i.e., the spatial properties of eigenvectors are mixed). In general, as  $\alpha_c$  decreases, the G mode eigenvector loading in the partially convecting region is diminished, and may even change sign. The PC mode, on the other hand, tends to have opposite loadings in the partially and fully convecting regions, with the loading in the latter region decreasing as  $\alpha_c$  decreases.

#### b. A two-box model for the G and PC modes

The case for which the PC and G decay times are much slower than the LC decay time scales is relevant to the passively coupled tropical ocean–atmosphere system. We exploit the separation of LC eigenvalues to replace the arbitrary  $N$ -box model by a simple  $N = 2$  system. Box 1, with an area size fraction  $f_1$ , is fully convecting, while box 2, with an area size fraction  $f_2 = 1 - f_1$ , has specified convective fraction  $\alpha_c$  as in the  $N$ -box case. As with the prototype of section 4, strict QE and constant gross moist stability  $M$  are applied in

box 1 and the convecting portion of box 2. SSTAs imposed in box 2 are assumed not to alter  $\alpha_c$ .

Although this model can be treated as a literal two-box model, its true utility lies in its capacity to approximate the  $N$ -box model closely in certain parameter ranges, eliminating redundant degenerate solutions. Furthermore, its straightforward analytic solution elucidates the behavior of the G and PC modes. Specifically,

- The two-box solutions approximate the G and PC modes over a large range of parameters (i.e.,  $f_1$  greater than roughly 0.3, and small to modest  $\alpha_c$ ). In the  $N$ -box case, the set of convecting-region boxes is characterized by identical eigenvector loadings for the G and PC modes and may thus be replaced by box 1 in the two-box model. This gives an excellent approximation to these two modes, as seen in Fig. 5b. The case  $f_1 = 0.75$  may be compared to the numerical case in Fig. 5a, with the caveat that the differences seen are the result of using nonzero  $\tau_c$  in the latter. (Note that the degenerate LC modes in Fig. 5b are obtained in a separate calculation; see the third bullet.)
- Analysis of the PC region time scale in the nonconvecting ( $\alpha_c = 0$ ) limit provides insight into why the partially convecting region exhibits slow decay.
- Other limits of the two-box model are useful for other purposes (e.g., for  $f_1$  small and  $\alpha_c = 1$ , the two-box model yields the G and LC modes).

Analytic expressions for steady-state  $T$ ,  $q$ , and  $\nabla \cdot \mathbf{v}$  in the two-box framework are outlined in appendix B. Here we note that the  $2 \times 2$  surface flux sensitivity matrix to unit SSTAs is

$$\mathbf{G} = \begin{bmatrix} \epsilon_{T_s}^{T_s} + (\epsilon_{T_s}^{T_s} + \beta \epsilon_q^{T_s})T(1, 0) & \epsilon_{T_s}^{T_s}T(1, 0) + \epsilon_q^{T_s}q_2(1, 0) \\ (\epsilon_{T_s}^{T_s} + \beta \epsilon_q^{T_s})T(0, 1) & \epsilon_{T_s}^{T_s} + \epsilon_{T_s}^{T_s}T(0, 1) + \epsilon_q^{T_s}q_2(0, 1) \end{bmatrix}, \quad (13)$$

where  $T(1, 0)$  and  $T(0, 1)$  are tropospheric temperature perturbation associated with unit SSTAs in boxes 1 and 2, respectively, and  $q_2(1, 0)$  and  $q_2(0, 1)$  are box 2 moisture values for the same cases. The eigenvalues of (13) are simply  $\lambda_{\pm} = \frac{1}{2}(G_{11} + G_{22}) \pm \frac{1}{2}D^{1/2}$ , where the discriminant  $D$  is given by  $D = (G_{11} - G_{22})^2 + 4G_{12}G_{21}$ .

Some insight into the behavior of the eigenvalues can be obtained by examining the behavior of the diagonal and off-diagonal matrix elements of  $\mathbf{G}$  (Fig. 6). Consider parameters values for which the squared difference between diagonal elements (Fig. 6a) is large compared to the product of the off-diagonal terms. Then, the eigenvalues are approximately given by  $G_{11}$  and  $G_{22}$ . The behavior of  $G_{11}$  is easily understood. In

the limit of vanishing  $f_1$ ,  $T(1, 0)$  is identically zero, so  $G_{11} = \epsilon_{T_s}^{T_s}$ . As  $\alpha_c$  increases,  $T(1, 0)$  increases (linearly), and since  $\epsilon_{T_s}^{T_s}$  and  $\epsilon_q^{T_s}$  are of opposite sign to  $\epsilon_{T_s}^{T_s}$ , the magnitude of  $G_{11}$  decreases. Thus, the two limits  $f_1 = 0$  and  $f_1 = 1$  correspond to the fast LC and slow G modal decay times, respectively.

As suggested by Fig. 6b, the off-diagonal terms  $G_{21}$  and  $G_{12}$  are generally small for the parameter values assumed here, especially  $G_{21}$ , which represents the effect of partially convecting-region SSTA on the fully convecting region. The smallness of the off-diagonal terms explains why the eigenvector loadings of the G and PC modes are small in the partially and fully convecting regions, respectively. As Fig. 6a further indi-

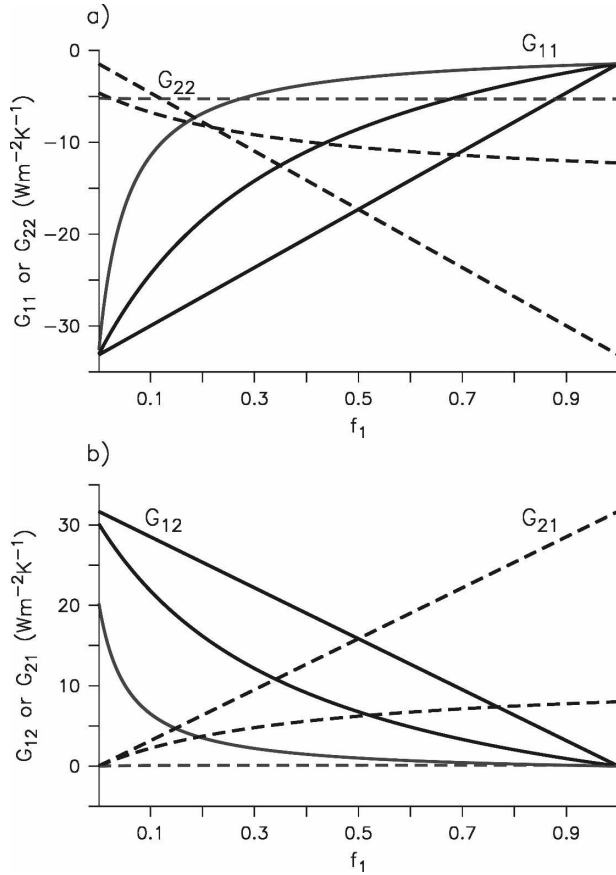


FIG. 6. (a) Diagonal and (b) off-diagonal matrix elements of  $\mathbf{G}$  for the analytic two-box model as a function of box 1 area fraction  $f_1$ . Solid (dashed) lines in (a), (b) denote  $G_{11}$  or  $G_{12}$  ( $G_{22}$  or  $G_{21}$ ). Black, dark gray, and light gray lines correspond to box 2 convective fraction values  $\alpha_c$  of 1.0, 0.25, and 0.0, respectively. The diagonal elements give the local decay tendencies in the fully convecting and partially convecting regions, respectively;  $G_{21}$  gives the effect of SSTA in the fully convecting region on surface flux in the partially convecting region, while  $G_{12}$  gives the (typically much smaller) converse.

cates, the diagonal terms  $G_{11}$  and  $G_{22}$  may approach one another; in this case, the off-diagonal terms may significantly modify the eigenvalues.

For the parameter values assumed,  $G_{12}$  and  $G_{21}$  are positive, so both terms in the discriminant  $D$  are positive. However, under certain circumstances, the flux perturbation in the PC region to, say, a positive SST perturbation in the fully convecting regions may result in  $G_{21}$  changing sign. This occurs because (i) on the one hand, tropospheric temperature increases over the partially convecting region, leading to enhanced longwave warming of the surface; (ii) while on the other hand, descent anomalies suppress moisture, thereby increasing evaporation, which has a cooling tendency. The

TABLE 2. Flux sensitivity parameters.

Symbol	Value
$a$	0.66
$b$	3.17
$\gamma$	3.5 K K <sup>-1</sup>
$\epsilon_H$	5.97 W m <sup>-2</sup> K <sup>-1</sup>
$\epsilon_T^{\text{surf}}$	-2.81 W m <sup>-2</sup> K <sup>-1</sup>
$\epsilon_q^{\text{surf}}$	-8.21 W m <sup>-2</sup> K <sup>-1</sup>
$\epsilon_{T_s}^{\text{surf}}$	6.28 W m <sup>-2</sup> K <sup>-1</sup>
$\epsilon_T^{\text{toa}}$	2.91 W m <sup>-2</sup> K <sup>-1</sup>
$\epsilon_q^{\text{toa}}$	-2.55 W m <sup>-2</sup> K <sup>-1</sup>
$\epsilon_{T_s}^{\text{toa}}$	0.54 W m <sup>-2</sup> K <sup>-1</sup>

competition between warming and drying determines the sign of  $G_{21}$ .

For the nonconvecting limit  $\alpha_c = 0$ , the main case of interest, the matrix elements in Fig. 6 are relatively insensitive to  $f_1$  when  $f_1 > \sim 0.3$ . Therefore, the behavior of a small nonconvecting region ( $f_1 \rightarrow 1$ ) is a good prototype for that of one that represents even a modest fraction of the total tropical domain.

### c. Why nonconvecting regions exhibit slow decay

The strict QE assumption means that tropospheric temperature and humidity vary in concert, but even for finite convective adjustment time scales, convecting-region  $T$  and  $q$  anomalies must vary closely on time scales relevant to SST decay. The behavior of  $G_{22}$  is distinct from  $G_{11}$  since the  $T$  and  $q$  perturbations in box 2 become less tightly coupled as  $\alpha_c$  decreases. Take the case of  $\alpha_c = 0$  SSTA imposed in box 2. The box 2 moisture equation in the nonconvecting limit is just  $\overline{M}_q^{\text{nc}} \nabla \cdot \mathbf{v}_2 + M_{qp} \nabla \cdot \overline{\mathbf{v}}^{\text{nc}} q_2 + E = 0$ , where the superscript “nc” denotes nonconvecting values and the moisture stratification  $M_q$  has been expanded as  $M_q = \overline{M}_q + M_{qp} q$ , with  $M_{qp}$  representing moisture stratification per unit  $q$ . When the nonconvecting region is relatively small,  $f_2 \rightarrow 0$ ,  $T(0, 1) = 0$ ,

$$\nabla \cdot \mathbf{v}_2 = \overline{M}_s (\epsilon_{T_s}^T T_{s2} + \epsilon_q^T q_2), \quad (14)$$

so

$$q_2 = \frac{\gamma \epsilon_H + \overline{M}_q \overline{M}_s^{-1} \epsilon_{T_s}^T}{b \epsilon_H - M_{qp} \nabla \cdot \overline{\mathbf{v}}^{\text{nc}} - \overline{M}_q \overline{M}_s^{-1} \epsilon_q^T} T_{s2}. \quad (15)$$

Even though there is no temperature perturbation,  $q_2(0, 1)$  is nonzero and positive (since both numerator and denominator are positive) since it rises with evaporation until balance is achieved.

For the parameter values given in Table 2, the first terms in both the numerator and denominator of (15) are roughly 2–3 times as large as the remaining terms.

Expanding the denominator to first order in terms small compared to  $b\epsilon_H$ ,  $q_2$  becomes

$$q_2 \approx (\gamma/b)[1 + (M_{qp}\nabla \cdot \bar{\mathbf{v}}^{\text{nc}})/(b\epsilon_H) + (M_q\epsilon_{T_s}^T/M_s)/(\gamma\epsilon_H) + (M_q\epsilon_q^T/M_s)/(b\epsilon_H)]. \quad (16)$$

The latent heating, sensible heating, and net surface radiative components of the total surface heat flux for the nonconvecting region (i.e.,  $G_{22}$ ) are

$$E \approx -[(\gamma M_{qp}/b)\nabla \cdot \bar{\mathbf{v}}^{\text{nc}} + (M_q/M_s)(\epsilon_{T_s}^{\text{surf}} - \epsilon_{T_s}^{\text{toa}} + \epsilon_H) + (\gamma/b)(M_q/M_s)(\epsilon_q^{\text{surf}} - \epsilon_q^{\text{toa}})]T_{s2}, \quad (17)$$

$$H = \epsilon_H T_{s2}, \quad (18)$$

$$R_s \approx [\epsilon_{T_s}^{\text{surf}} + \epsilon_q^{\text{surf}}(\gamma/b)]T_{s2}. \quad (19)$$

The evaporation comprises contributions from (slow) mean subsidence [the first term on the rhs of (17)] as well as feedback terms associated with changes to circulation. The contribution of the mean subsidence term, which is the largest single component of the net surface flux, implies  $E \propto$  moisture divergence. The remaining terms are associated with atmospheric absorption of anomalous fluxes from the surface, which lead to anomalous ascent opposing the climatological descent. The resulting decrease in evaporation tends to partially compensate for upward surface fluxes, for example, longwave radiation and sensible heat flux, Eqs. (18) and (19), that act to cool SST. As an example, consider the effect of the term associated with upward longwave radiative cooling of the surface associated with the direct effect of anomalously warm SSTA [the first term on the rhs of (19)]. Writing the portion of emitted longwave radiation absorbed by the atmosphere as  $\delta = (\epsilon_{T_s}^s - \epsilon_{T_s}^l)/\epsilon_{T_s}^s$ , the net cooling when including the feedback effect in evaporation reduces the direct longwave cooling by a factor of approximately  $(1 - \bar{M}_q \bar{M}_s^{-1} \delta)$ . Since  $M_q$  is a large fraction of  $M_s$  and a large fraction of longwave is absorbed, this amounts to a substantial reduction. Similar arguments apply to the longwave flux associated with changes to moisture as well as the sensible heating.

For a small nonconvecting region, the rate of evaporative cooling is limited by the slow moisture divergence; other forms of surface cooling are reduced by feedbacks via the circulation onto evaporation. This results in a much slower decay than for a small convecting region. An alternative perspective on the slowness of nonconvecting-region decay was developed by Chiang and Sobel (2002). Specifically, in the absence of deep convection, the communication between the free tropospheric temperature and the surface is limited, since the time scale for vertical advective transport is much

slower than the time scale for vertical convective transport. Because  $q$  and  $T$  are effectively decoupled within nonconvecting regions, the former can buffer surface temperature from the free tropospheric temperature, which restricts the capacity for SSTA decay.

The behavior of  $G_{22}$  further suggests that nonconvecting-region decay times should barely change as the size of the nonconvecting region is varied (for a region with small  $\alpha_c$ ). This is because there is no convective feedback on the warming by surface fluxes, so  $T$  remains small, and the balances remain similar to the analysis for small  $f_2$ .

#### d. Merger of the G and NC modes

Previously, we noted the role of horizontal transports in setting decay time scales, particularly for the most slowly decaying modes. For the results displayed in Fig. 5, the damping coefficients  $\epsilon_T^{\text{tr}}$  and  $\epsilon_q^{\text{tr}}$ , representing transport to the extratropics, are set to zero, resulting in rather long (>1000 day) decay times for the G mode. However, small changes to these damping coefficients can have a strong impact on the eigenvalues: in Fig. 7a, the two damping coefficients (assumed equal for simplicity) were varied over a realistic range of values for  $f_1 = 0.6$  for  $\alpha_c = 0$ . By increasing, say, the  $T$  damping, the tropospheric temperature warming is lowered relative to the no-damping situation; this results in a decrease in  $G_{11}$  ( $G_{22}$  also decreases, but the change is less pronounced). Thus, the nonconvecting-region mode and global decay mode eigenvalues increase—and in fact converge—as the damping increases.

For zero damping and  $f_1 = 0.6$ ,  $G_{12}$  and  $G_{21}$  are both small, so the off-diagonal terms have little impact on the eigenvalues. However, the convergence of diagonal matrix elements as damping increases means that the off-diagonal terms may become more significant. In fact, as the damping increases beyond  $\epsilon_T^{\text{tr}} \approx 0.3$ , the sign of  $G_{21}$  changes for the reason discussed in section 5b. The discriminant changes sign when  $(G_{11} - G_{22})^2$  becomes less than  $4G_{12}G_{21}$ . Thus, a complex conjugate pair replaces the two real eigenvalues for damping values greater than  $\epsilon_T^{\text{tr}} \approx 1.85 \text{ W m}^{-2} \text{ K}^{-1}$ .

This case provides a simple illustration of the blending of properties that may occur between eigenmodes. This can occur even if the eigenvalues do not become equal, as in the case shown, but simply become sufficiently close to one another. In particular, the properties of the G mode—which for physically realistic climatologies is the most slowly decaying mode characterized by the broadest spatial scale—become mixed with the properties of slowly decaying PC modes. This behavior can account for some of the spatial inhomogeneity seen in the eigenvalue analysis of the full QTCM1

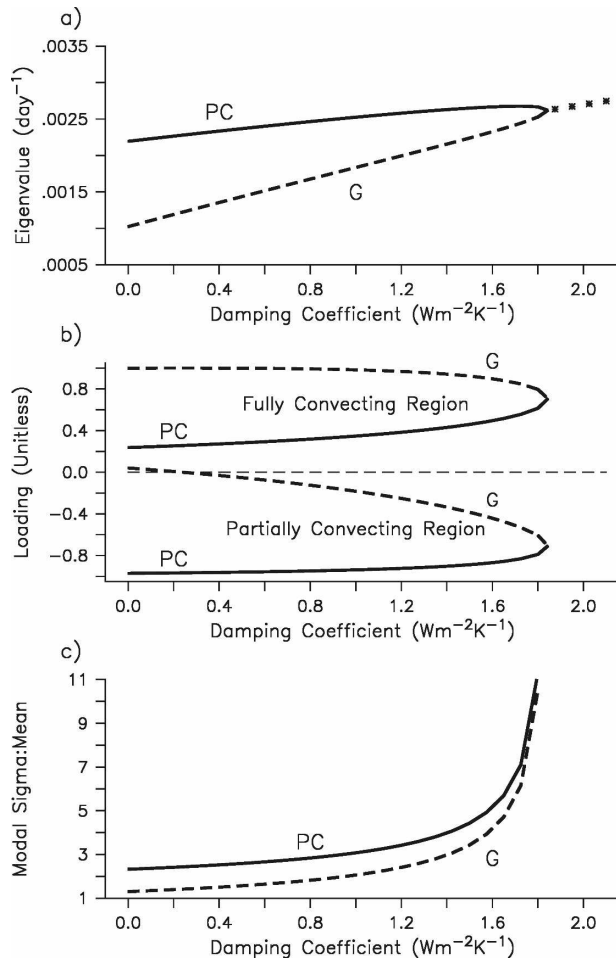


FIG. 7. Eigenmode properties as a function of horizontal transport/damping coefficients  $\epsilon_r^T$  and  $\epsilon_q^T$ . The case shown corresponds to  $f_1 = 0.6$  and  $\alpha_c = 0$ , that is, the partially convecting region is nonconvecting, with  $\epsilon_r^T = \epsilon_q^T$ . (a) Eigenvalues ( $\text{day}^{-1}$ ) for the PC mode (solid line) and G mode (dashed line). Note that for values of coefficients exceeding  $1.84 \text{ W m}^{-2} \text{ K}^{-1}$ , the eigenvalues comprise a complex conjugate pair. (b) Eigenvalue loadings for the two modes in the fully convecting region (top two curves) and the partially convecting region (bottom two curves). (c) Ratios of eigenvector standard deviations to eigenvector means for the two modes.

simulations (section 3). The regions of slowest local decay appear with high loadings in the slow global mode of the tropical case because of this blending effect, since the time scales are not well separated. The slow nonconvecting regions can appear with either sign in the G mode for either of two reasons. One is if the effect of convecting-region SSTA actually creates a cooling in the nonconvecting region, as noted above. The other, as seen for instance in Fig. 3, is simply that if there is more than one slow decay region, they will tend to occur with opposite sign in the leading eigenmodes.

## 6. Summary and conclusions

The spatial inhomogeneity of SSTA autocorrelation times in atmospheric models (CCM3 and QTCM1), when coupled to an ocean mixed layer, motivates a systematic study of the modes of the passively coupled system. When inhomogeneity is ignored, the physics underlying the local and global decay time scales is straightforward. For small-scale SSTA anomalies, decay times are typically rapid, with  $e$ -folding times of the order 50–100 days for a 50-m mixed layer. Because the atmospheric response to a localized heating anomaly is spread by transport over large distances, mixed layer heat content is rapidly extracted from sufficiently localized anomalies. As the areal extent of the SSTA increases, the decay rate becomes progressively limited by relatively slow top-of-the-atmosphere radiative transfer. Consequently, for a global SSTA, for which the size of the anomaly is comparable to the total radiating area of the atmosphere, the decay time for a 50-m mixed layer exceeds 500 days.

Under more realistic conditions, the transition between the fast local and slow global scales is nontrivial. Within the tropics, efficient horizontal wave dynamics communicates the heating from local sources over the extent of the equatorial waveguide,  $\sim 20^\circ\text{S}$ – $20^\circ\text{N}$ . Eigenvalue analysis applied to idealized simulations of QTCM1 indicates that local decay is a reasonable approximation for spatial scales smaller than either the tropical Atlantic or Indian Ocean basins. Extratropical wave dynamics also affects SST decay characteristics, although in a more complicated way (e.g., nonlinearities associated with midlatitude wave dynamics impart a nontrivial structure to the passive decay characteristics).

A major focus of this study concerned the impact of basic-state climate on tropical decay characteristics. In this vein, we noted the distinct separation of local tropical SST decay time scales for mean convecting and nonconvecting regions, with the latter exhibiting decay time scales several times longer than the former. The reasons for such separation were highlighted in section 5: for nonconvecting regions, the dominant balance is between slow moisture divergence via the subsiding mean flow and evaporation. In the absence of a convective moisture sink, sizable tropospheric humidity anomalies develop in response to SSTAs imposed within the nonconvecting region: these anomalies limit the rate of evaporation to a value given by the slow moisture divergence, in turn implying a slow rate of SST decay. Longwave radiation emitted by the surface is substantially absorbed in the atmosphere, which

slows moisture divergence, and therefore has a limited impact on SSTA decay characteristics.

The slow decay of nonconvecting regions has significant implications for the spatial structure of passive ocean–atmosphere decay modes, especially the slowly decaying global mode. While the global decay mode might be expected to exhibit a broad, uniform spatial structure, this assumption does not hold in the presence of basic-state inhomogeneities: although eigenvalue analysis indicates a relatively broad structure for the most slowly decaying mode, it is spatially heterogeneous. In particular, the features of the global decay mode are blended or mixed with the localized, slow decay characteristics of nonconvecting areas. Precisely how this blending affects the eigenmodes depends sensitively on a number of factors (e.g., the closeness of decay mode time scales), and the loading of slowest decay mode in the nonconvecting region can have relatively small or large amplitude or even change sign. If the nonconvecting and global mode time scales approach each other, a merger may even occur. In the eigenvalue analysis of QTCM1, the most visible signature is large eigenvector loadings of the slow, leading eigenmodes in localized slowly decaying regions.

Although we have framed our analysis largely in terms of the decay of SSTAs, the results also apply to passive mixed layer equilibration to a prescribed climate forcing (e.g., the remote tropical climate response to El Niño or the transient upper ocean adjustment to atmospheric radiative anomalies associated with greenhouse gases or aerosols). For instance, SNM05 argued that tropical tropospheric warming to El Niño can be viewed in two stages: a fast stage, associated with energy loss to the unadjusted remote mixed layer, and a slower stage—essentially the global tropical decay time scale—limited by top-of-the-atmosphere radiative losses and tropical–extratropical energy export.

The results of our study add a further layer of complexity to the picture of the tropospheric temperature adjustment to El Niño, specifically with respect to the impacts of basic-state inhomogeneities. Consider, for example, the tropical Atlantic. Because of the Northern Hemisphere bias of the intertropical convergence zone, the north tropical Atlantic is, on average, more strongly convecting than the south tropical Atlantic. Thus, we anticipate modifications to the rate of tropospheric warming from the local convective and nonconvective region decay modes operating to the north and south of the equator, respectively. We thus conjecture that the inhomogeneous passive decay modes examined here may be useful ingredients in understanding the observed tendency for an equatorially asymmetric tropical Atlantic surface temperature response to El Niño, with

regions north of the equator warming more, and with different timing, than those to the south (Enfield and Mayer 1997; Elliott et al. 2001; Chiang and Sobel 2002). Equally intriguing, and warranting further study, is how the slow decay region in the nonconvecting southeastern tropical Pacific, encountered here with only passive coupling, interacts with ocean dynamics in the ENSO source region.

*Acknowledgments.* We thank J. C. H. Chiang for providing the CCM3 mixed layer simulation. We also thank J. T. Farrar, C. Holloway, A. H. Sobel, J. Nilsson, and two anonymous reviewers for valuable discussion and comments on the manuscript. This work was supported in part by NOAA Grants NA04OAR4310013 and NA05OAR4310007 and NSF Grant ATM-0645200. BRL further acknowledges partial support by J. C. H. Chiang and NOAA Grant NA03OAR4310066.

## APPENDIX A

### Flux Sensitivity Coefficients

The flux sensitivity coefficients are defined analogously to SNM05. The values assumed are representative of clear-sky conditions. These coefficients are

$$\epsilon_{T_s}^T = \epsilon_{T_s}^{\text{surf}} + \gamma\epsilon_H + \epsilon_H, \quad (\text{A1})$$

$$\epsilon_q^T = b\epsilon_H + \epsilon_q^{\text{surf}}, \quad (\text{A2})$$

$$\epsilon_T^T = a\epsilon_H + \epsilon_T^{\text{surf}}, \quad (\text{A3})$$

$$\epsilon_{T_s}^T = \epsilon_H + \epsilon_{T_s}^{\text{surf}} - \epsilon_{T_s}^{\text{toa}}, \quad (\text{A4})$$

$$\epsilon_{T_s}^q = \gamma\epsilon_H, \quad (\text{A5})$$

$$\epsilon_T^T = \epsilon_T^{\text{surf}} - \epsilon_T^{\text{toa}} - a\epsilon_H - \epsilon_T^{\text{tr}}, \quad (\text{A6})$$

$$\epsilon_q^T = \epsilon_q^{\text{surf}} - \epsilon_q^{\text{toa}}, \quad (\text{A7})$$

$$\epsilon_T^q = 0, \quad \text{and} \quad (\text{A8})$$

$$\epsilon_q^q = -b\epsilon_H - \epsilon_q^{\text{tr}}. \quad (\text{A9})$$

In the above expressions,  $a$  and  $b$  relate the QTCM1 vertical structure functions of temperature and moisture to their surface values, respectively. The coefficient  $\gamma$ , defined as  $\partial q_s / \partial T_s$ , where  $q_s$  is saturation specific humidity at the surface, follows from the linearization of evaporation; it is evaluated with respect to a reference temperature, taken here to be 302 K. Values of the flux sensitivity parameters are summarized in Table 2. The temperature and moisture transport coefficients,  $\epsilon_T^{\text{tr}}$  and  $\epsilon_q^{\text{tr}}$ , are treated as adjustable parameters.

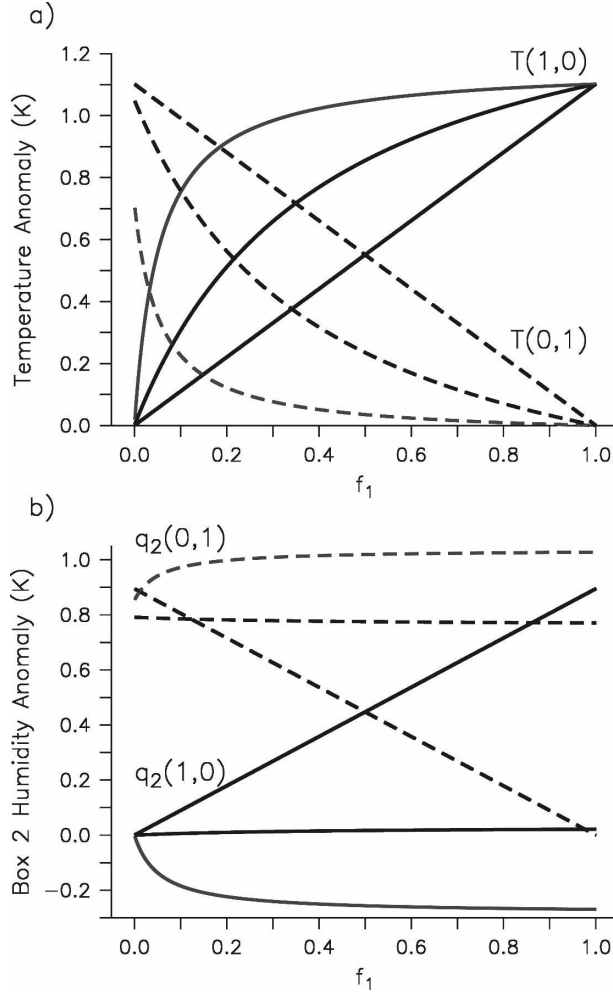


FIG. B1. (a) Tropospheric temperature and (b) box 2 humidity anomalies for the analytic two-box model as a function of box 1 area fraction  $f_1$ . Solid lines are for an imposed 1-K SST perturbation in box 1 (the fully convecting region), and dashed lines are for an imposed 1-K SST perturbation in box 2 (the partially convecting region). Black, dark gray, and light gray lines correspond to box 2 convective fraction values  $\alpha_c$  of 1.0, 0.25, and 0.0, respectively.

## APPENDIX B

### Analytic Solutions to the Two-Box Model

Using the labeling conventions of section 6, the temperature perturbation to an arbitrary distribution of SSTs  $T_{s1}$  and  $T_{s2}$  is

$$T(T_{s1}, T_{s2}) = T^* \{ \bar{M}^{c-1} (f_1 + f_2 \alpha_c) [\epsilon_T^T + \beta (\epsilon_q^T + \epsilon_q^q)] + (1 - \alpha_c) f_2 \epsilon_T^T C_1 \}^{-1}, \quad (\text{B1})$$

where

$$T^* = -[\bar{M}^{c-1} (\epsilon_T^T + \epsilon_T^q) (f_1 T_{s1} + f_1 \alpha_c T_{s2}) + (1 - \alpha_c) f_2 C_1 C_2 T_{s2}] \quad \text{and}$$

$$C_1 = \left[ \bar{M}_s^{nc} + \frac{\epsilon_q^T \bar{M}_q^{nc}}{M_{qp} \nabla \cdot \bar{\mathbf{v}}^{nc} + \epsilon_q^q} \right]^{-1} \quad \text{and}$$

$$C_2 = \epsilon_{T_s}^T - \frac{\epsilon_q^T \epsilon_{T_s}^q}{M_{qp} \nabla \cdot \bar{\mathbf{v}}^{nc} + \epsilon_q^q}.$$

For box 1, the humidity perturbation is, by the strict QE assumption, just  $q_1(T_{s1}, T_{s2}) = \beta T(T_{s1}, T_{s2})$ . For box 2, on the other hand,

$$q_2(T_{s1}, T_{s2}) = \alpha_c \beta T - (1 - \alpha_c) (\epsilon_{T_s}^q T_{s2} + \bar{M}_q^{nc} \nabla \cdot \bar{\mathbf{v}}_2) \times (M_{qp} \nabla \cdot \bar{\mathbf{v}}^{nc} + \epsilon_q^q)^{-1}, \quad (\text{B2})$$

where  $\nabla \cdot \bar{\mathbf{v}}_2(T_{s1}, T_{s2}) = C_1 [C_2 T_{s2} + \epsilon_T^T (f_1, \alpha_c)]$ . Plots of the temperature and humidity anomalies in response to separate 1-K SST perturbations in each box are illustrated in Fig. B1.

## REFERENCES

- Alexander, M. A., I. Bladé, M. Newman, J. R. Lanzante, N.-C. Lau, and J. D. Scott, 2002: The atmospheric bridge: The influence of ENSO teleconnections on air-sea interaction over the global oceans. *J. Climate*, **15**, 2205–2231.
- Barsugli, J. J., and D. S. Battisti, 1998: The basic effects of atmosphere-ocean thermal coupling on midlatitude variability. *J. Atmos. Sci.*, **55**, 477–493.
- Battisti, D. S., 1988: Dynamics and thermodynamics of a warming event in a coupled tropical atmosphere-ocean model. *J. Atmos. Sci.*, **45**, 2889–2919.
- Betts, A. K., and M. J. Miller, 1986: A new convective adjustment scheme. Part II: Single column tests using GATE wave, BOMEX, ATEX and Arctic air-mass data sets. *Quart. J. Roy. Meteor. Soc.*, **112**, 693–709.
- Bhatt, U. S., M. A. Alexander, D. S. Battisti, D. D. Houghton, and L. M. Keller, 1998: Atmosphere-ocean interaction in the North Atlantic: Near-surface climate variability. *J. Climate*, **11**, 1615–1632.
- Bretherton, F. P., 1982: Ocean climate modeling. *Prog. Oceanogr.*, **11**, 93–129.
- Cane, M. A., and S. E. Zebiak, 1986: On the mechanism of the El Niño-Southern Oscillation cycle. *Study Week on Persistent Meteorological Anomalies and Teleconnections*, C. Chagas and G. Puppi, Eds., Pontificia Academia Scientiarum, 6–96.
- Chang, P., L. Ji, H. Li, C. Penland, and L. Matrosova, 1998: Prediction of tropical Atlantic sea surface temperature. *Geophys. Res. Lett.*, **25**, 1193–1196.
- Chiang, J. C. H., and A. H. Sobel, 2002: Tropical tropospheric temperature variations caused by ENSO and their influence on the remote tropical climate. *J. Climate*, **15**, 2616–2631.
- , and B. R. Lintner, 2005: Mechanisms of remote tropical surface warming during El Niño. *J. Climate*, **18**, 4130–4149.
- Chou, C., and J. D. Neelin, 2004: Mechanisms of global warming impacts on regional tropical precipitation. *J. Climate*, **17**, 2688–2701.
- , —, J.-Y. Tu, and C.-T. Chen, 2006: Regional tropical precipitation change mechanisms in ECHAM4/OPYC3 under global warming. *J. Climate*, **19**, 4207–4223.

- Deser, C., M. A. Alexander, and M. S. Timlin, 2003: Understanding the persistence of sea surface temperature anomalies in midlatitudes. *J. Climate*, **16**, 57–72.
- Efron, B., 1982: *The Jackknife, the Bootstrap, and Other Resampling Plans*. Society for Industrial and Applied Mathematics, 92 pp.
- Elliott, J. R., S. P. Jewson, and R. T. Sutton, 2001: The impact of the 1997/98 El Niño event on the Atlantic Ocean. *J. Climate*, **14**, 1069–1077.
- Enfield, D. B., and D. A. Mayer, 1997: Tropical Atlantic sea surface temperature variability and its relation to El Niño–Southern Oscillation. *J. Geophys. Res.*, **102**, 929–945.
- Frankignoul, C., 1985: Sea surface temperature anomalies, planetary waves, and air–sea feedback in the middle latitudes. *Rev. Geophys.*, **23**, 357–390.
- , and K. Hasselmann, 1977: Stochastic climate models. II: Application to sea-surface temperature anomalies and thermocline variability. *Tellus*, **29**, 289–305.
- Gallego, B., and P. Cessi, 2001: Decadal variability of two oceans and an atmosphere. *J. Climate*, **14**, 2815–2832.
- Giannini, A., J. C. H. Chiang, M. A. Cane, Y. Kushnir, and R. Seager, 2001: The ENSO teleconnection to the tropical Atlantic Ocean: Contributions of the remote and local SSTs to rainfall variability in the tropical Americas. *J. Climate*, **14**, 4530–4544.
- Grabowski, W. W., 2006: Impact of explicit atmosphere–ocean coupling on MJO-like coherent structures in idealized aquaplanet simulations. *J. Atmos. Sci.*, **63**, 2289–2306.
- Hansen, J., and Coauthors, 1997: Forcings and chaos in interannual to decadal climate change. *J. Geophys. Res.*, **102**, 25 679–25 720.
- Hasselmann, K., 1976: Stochastic climate models. Part I: Theory. *Tellus*, **28**, 473–485.
- Kara, A. B., P. A. Rochford, and H. E. Hurlburt, 2003: Mixed layer depth variability over the global ocean. *J. Geophys. Res.*, **108**, 3079, doi:10.1029/2000JC000736.
- Kiehl, J. T., J. J. Hack, G. B. Bonan, B. A. Boville, D. L. Williamson, and P. J. Rasch, 1998: The National Center for Atmospheric Research Community Climate Model: CCM3. *J. Climate*, **11**, 1131–1149.
- Klein, S. A., B. J. Soden, and N.-C. Lau, 1999: Remote sea surface temperature variations during ENSO: Evidence for a tropical atmospheric bridge. *J. Climate*, **12**, 917–932.
- Kushnir, Y., W. A. Robinson, I. Bladé, N. M. J. Hall, S. Peng, and R. Sutton, 2002: Atmospheric GCM response to extratropical SST anomalies: Synthesis and evaluation. *J. Climate*, **15**, 2233–2256.
- Lin, J. W.-B., J. D. Neelin, and N. Zeng, 2000: Maintenance of tropical intraseasonal variability: Impact of evaporation–wind feedback and midlatitude storms. *J. Atmos. Sci.*, **57**, 2793–2823.
- Maloney, E. D., and A. H. Sobel, 2004: Surface fluxes and ocean coupling in the tropical intraseasonal oscillation. *J. Climate*, **17**, 4368–4386.
- Marotzke, J., and D. W. Pierce, 1997: On spatial scales and lifetimes of SST anomalies beneath a diffusive atmosphere. *J. Phys. Oceanogr.*, **27**, 133–139.
- Marshall, J., and Coauthors, 2001: North Atlantic climate variability: Phenomena, impacts and mechanisms. *Int. J. Climatol.*, **21**, 1863–1898.
- Münnich, M., M. Latif, S. Venzke, and E. Maier-Reimer, 1998: Decadal oscillations in a simple coupled model. *J. Climate*, **11**, 3309–3319.
- Neelin, J. D., and W. Weng, 1999: Analytical prototypes for ocean–atmosphere interaction at midlatitudes. Part I: Coupled feedbacks as a sea surface temperature dependent stochastic process. *J. Climate*, **12**, 697–721.
- , and N. Zeng, 2000: A quasi-equilibrium tropical circulation model—Formulation. *J. Atmos. Sci.*, **57**, 1741–1766.
- , and H. Su, 2005: Moist teleconnection mechanisms for the tropical South American and Atlantic sector. *J. Climate*, **18**, 3928–3950.
- , D. S. Battisti, A. C. Hirst, F.-F. Jin, Y. Wakata, T. Yamagata, and S. E. Zebiak, 1998: ENSO theory. *J. Geophys. Res.*, **103**, 14 261–14 290.
- Nilsson, J., 2000: Propagation, diffusion, and decay of SST anomalies beneath an advective atmosphere. *J. Phys. Oceanogr.*, **30**, 1505–1513.
- , 2001: Spatial reorganization of SST anomalies by stationary atmospheric waves. *Dyn. Atmos. Oceans*, **34**, 1–21.
- Park, S., C. Deser, and M. A. Alexander, 2005: Estimation of the surface heat flux response to sea surface temperature anomalies over the global oceans. *J. Climate*, **18**, 4582–4599.
- Philander, S. G. H., T. Yamagata, and R. C. Pacanowski, 1984: Unstable air–sea interactions in the tropics. *J. Atmos. Sci.*, **41**, 604–613.
- Saravanan, R., and P. Chang, 2000: Interaction between tropical Atlantic variability and El Niño–Southern Oscillation. *J. Climate*, **13**, 2177–2194.
- Schopf, P. S., 1985: Modeling tropical sea-surface temperature: Implication of various atmospheric responses. *Coupled Ocean–Atmosphere Models*, J. C. J. Nihoul, Ed., Elsevier, 727–734.
- Sobel, A. H., and H. Gildor, 2003: A simple time-dependent model of SST hot spots. *J. Climate*, **16**, 3978–3992.
- Su, H., J. D. Neelin, and J. E. Meyerson, 2003: Sensitivity of tropical tropospheric temperature to sea surface temperature forcing. *J. Climate*, **16**, 1283–1301.
- , —, and —, 2005: Mechanisms for lagged atmospheric response to ENSO SST forcing. *J. Climate*, **18**, 4195–4215.
- Tang, B. H., and J. D. Neelin, 2004: ENSO influence on Atlantic hurricanes via tropospheric warming. *Geophys. Res. Lett.*, **31**, L24204, doi:10.1029/2004GL021072.
- Timlin, M. S., M. A. Alexander, and C. Deser, 2002: On the re-emergence of North Atlantic SST anomalies. *J. Climate*, **15**, 2707–2712.
- Watanabe, M., and M. Kimoto, 2000: On the persistence of decadal SST anomalies in the North Atlantic. *J. Climate*, **13**, 3017–3028.
- Wu, Z.-X., and R. E. Newell, 1998: Influence of sea surface temperatures on air temperatures in the tropics. *Climate Dyn.*, **14**, 275–290.
- Zeng, N., J. D. Neelin, and C. Chou, 2000: A quasi-equilibrium tropical circulation model—Implementation and simulation. *J. Atmos. Sci.*, **57**, 1767–1796.
- Zhang, C. D., M. Dong, S. Gualdi, H. H. Hendon, E. D. Maloney, A. Marshall, K. R. Sperber, and W. Q. Wang, 2006: Simulations of the Madden–Julian oscillation in four pairs of coupled and uncoupled global models. *Climate Dyn.*, **27**, 573–592.